



Article

Experimental and Computational Studies on Superhard Material Rhenium Diboride under Ultrahigh Pressures

Kaleb C. Burrage, Chia-Min Lin, Wei-Chih Chen, Cheng-Chien Chen *  and Yogesh K. Vohra * 

Department of Physics, University of Alabama at Birmingham (UAB), Birmingham, AL 35294, USA; kcburr@uab.edu (K.C.B.); lincm@uab.edu (C.-M.L.); weichih@uab.edu (W.-C.C.)

* Correspondence: chenc@uab.edu (C.-C.C.); ykvohra@uab.edu (Y.K.V.)

Received: 3 March 2020; Accepted: 31 March 2020; Published: 3 April 2020



Abstract: An emerging class of superhard materials for extreme environment applications are compounds formed by heavy transition metals with light elements. In this work, ultrahigh pressure experiments on transition metal rhenium diboride (ReB_2) were carried out in a diamond anvil cell under isothermal and non-hydrostatic compression. Two independent high-pressure experiments were carried out on ReB_2 for the first time up to a pressure of 241 GPa (volume compression $V/V_0 = 0.731 \pm 0.004$), with platinum as an internal pressure standard in X-ray diffraction studies. The hexagonal phase of ReB_2 was stable under highest pressure, and the anisotropy between the a -axis and c -axis compression increases with pressure to 241 GPa. The measured equation of state (EOS) above the yield stress of ReB_2 is well represented by the bulk modulus $K_0 = 364$ GPa and its first pressure derivative $K_0' = 3.53$. Corresponding density-functional-theory (DFT) simulations of the EOS and elastic constants agreed well with the experimental data. DFT results indicated that ReB_2 becomes more ductile with enhanced tendency towards metallic bonding under compression. The DFT results also showed strong crystal anisotropy up to the maximum pressure under study. The pressure-enhanced electron density distribution along the Re and B bond direction renders the material highly incompressible along the c -axis. Our study helps to establish the fundamental basis for anisotropic compression of ReB_2 under ultrahigh pressures.

Keywords: transition metal borides; superhard materials; high pressure studies; diamond anvil cell; ab initio calculations; elastic constants; crystal anisotropy

1. Introduction

Transition metal borides have shown intriguing mechanical and structural properties combining the attractive features of metallic bonding with rigid covalent boron-boron bonding [1–3]. In moving across the periodic table from a group IV transition metal boride like TiB_2 to a group VI transition metal boride like ReB_2 , the boron layer transitions from a planar hexagonal net to a more puckered structure. In particular, rhenium diboride (ReB_2) has shown desirable mechanical properties with a high average hardness of 30–60 GPa [4–7] and bulk modulus of 334–360 GPa [4,5], comparable to that of diamonds (442 GPa) [8]. Such materials are useful for their applicability under extreme conditions requiring a combination of high-temperature chemical stability and resistance to plastic deformation. Many superhard materials (hardness above 40 GPa) such as diamonds are prone to oxidation in high-temperature environments and have a propensity for chemical reactivity with transition metals. ReB_2 shows promise as an alternative to diamonds for mechanical uses due to strong covalent bonding between B - B and Re - B atoms and high electron density [4], the compound's stability up to 2000 K, and the ease of machining by electric discharge [9]. In this study, we investigate hexagonal ReB_2

compressed under non-hydrostatic conditions at ultrahigh pressure. Axial compression of the lattice parameters is investigated for the first time up to 241 GPa, and the equation of state is determined from the measured volume compression. ReB_2 shows strong crystal anisotropy and high incompressibility along the c -axis up to the maximum pressure. The experimental data are directly compared with first-principles simulations, showing good theory-experiment agreements. The scientific novelty of our work lies in combining ultrahigh-pressure X-ray diffraction experiments with density functional theory to gain fundamental understanding of anisotropic behavior.

2. Materials and Methods

Ultrahigh pressure was achieved by utilizing a diamond anvil cell (DAC) consisting of two diamonds facing each other in an opposed configuration (Figure 1a). The strong structural integrity of the diamond anvils allows for sample compressions to reach environments similar to those of deep planetary interiors and study material properties not seen at ambient conditions. In this study, two separate DACs were employed in an opposed anvil configuration with a 30-micron – 8-degree – 350-micron bevel for pressures to 241 GPa, and 100-micron – 7-degree – 300-micron anvils for pressures to 105 GPa. To minimize lateral flow of the sample material during compression, a steel gasket was indented to 25-micron thickness and a hole was laser drilled for sample placement on the culet. The sample hole sizes were made 8 microns for the 30-micron culet and 25 microns for the 100-micron culet. The ReB_2 sample from American Elements had a purity of 99.9% (metals basis) with major impurities of elemental Fe , Al , and Si in the 10 parts per million (ppm) range. The ReB_2 sample was mixed with Alfa-Aesar platinum powder (99.97% purity) for pressure calibration.

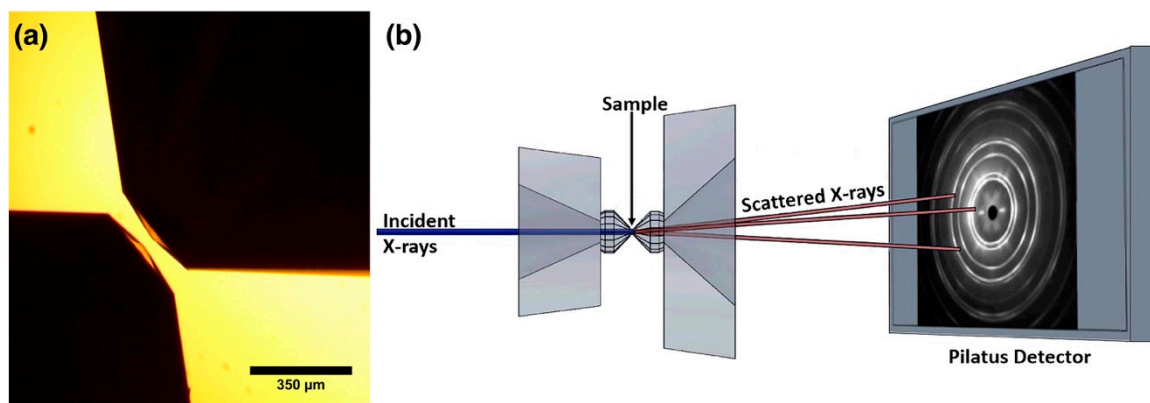


Figure 1. (a) Microscope image of two diamond anvils with an opposed configuration within a diamond anvil cell (DAC). Sample placement is centered on the culet, or flat tip, of one of the anvils. (b) Schematic of the DAC within experimental settings. Incident X-rays are propagated along the axis of compression and collected on a Pilatus 1M detector after sample scattering.

X-ray diffraction (XRD) experiments ($\lambda = 0.4133 \text{ \AA}$) were carried out on the High-Pressure Collaborative Access Team (HPCAT) Beamline 16-BM-D at the Advanced Photon Source in Argonne National Laboratory. As shown in Figure 1b, the X-ray beam was incident along the axis of compression, and scattered X-rays off the sample were captured on a Pilatus 1M detector with X-ray beam size $3.7 \mu\text{m}$ (vertical) \times $3.8 \mu\text{m}$ (horizontal) FWHM (full width at half maximum) and sample-to-detector distance of 344.63 mm calibrated using the CeO_2 diffraction profile in the Dioptas software. For more information on the optical components of the Beamline 16-BM-D, refer to Park et al. [10]. Structure refinements of lattice parameters were carried out using the GSAS-II software package [11]. The measured pressure-volume data for the sample were fitted to the 3rd order Birch–Murnaghan equation of state (EOS):

$$P(V) = \frac{3}{2}K_0 \left[x^{\frac{7}{3}} - x^{\frac{5}{3}} \right] \left[1 + \frac{3}{4}(K'_0 - 4) \left[x^{\frac{2}{3}} - 1 \right] \right] \quad (1)$$

Here, V is the measured volume at high pressure and V_0 is the ambient pressure volume with $x = V_0/V$; K_0 and K_0' are the bulk modulus and its first pressure derivative, respectively. To determine the initial volume V_0 of the ReB_2 sample, ambient pressure XRD measurements were separately recorded of the starting material, and the lattice parameters were determined to be $a_0 = 2.901 \text{ \AA}$ and $c_0 = 7.482 \text{ \AA}$. The platinum EOS used was calibrated up to 550 GPa from Yokoo et al. [12] using the 3rd order Birch–Murnaghan EOS and employed as a pressure marker using $K_0 = 276.4 \text{ GPa}$ and $K_0' = 5.12$ with the platinum lattice parameter $a = 3.924 \text{ \AA}$ at ambient pressure.

First-principles calculations are based on density functional theory (DFT) [13], which dictates that the ground state energy (or potential) of interacting electrons is a functional of charge density. The DFT potential is constructed as the sum of external potential due to atomic nuclei, which are seen as fixed by electrons within the Born–Oppenheimer approximation [14], and an effective potential due to electron interactions. The resulting electronic ground state is obtained by solving self-consistently one-electron Schrödinger-like equations known as Kohn–Sham equations [15]. Here, we used the DFT software VASP (Vienna Ab initio Simulation Package, version 5.4.4) [16,17], in which a plane-wave basis set and pseudopotential method are adopted. In our calculations, we employed the projector augmented wave (PAW) [18,19] method and the Perdew–Burke–Ernzerhof generalized gradient approximation (PBE-GGA) [20] functional. Charge carriers in the $Re:5d^66s^1$ and $B:2s^22p^1$ configurations were treated as valence electrons, and the valence wave functions were expanded in a plane wave basis up to a kinetic energy of 420 eV. The Monkhorst–Pack k-point sampling of the Brillouin zone [21] was chosen by a Γ -centered k-point mesh with a fine resolution $= 0.01 \times 2\pi/\text{\AA}$ ($33 \times 33 \times 13$). The convergence criteria for self-consistent field and structure relaxation were set to $10^{-6} \text{ eV/unit cell}$ and 10^{-3} eV/\AA , respectively. For each given external pressure point, we first performed a structure optimization calculation in the hexagonal phase with fully relaxed lattice parameters and atomic positions. The theoretical lattice parameters at ambient conditions are $a_0 = 2.913 \text{ \AA}$ and $c_0 = 7.504 \text{ \AA}$, which are within a 0.5% error margin compared to the corresponding experimental values. After the structure relaxation, we then performed calculations with lattice distortion to obtain the crystal's elastic tensor, which provided information on mechanical properties such as bulk and shear moduli, as well as crystal anisotropy. The bulk modulus computed by DFT with the Voigt–Reuss–Hill approximation [22] is $K_0 = 357 \text{ GPa}$ at ambient conditions, which agrees within a 2% error margin with the value $K_0 = 364 \text{ GPa}$ obtained by fitting the experimental P - V curve to the 3rd order Birch–Murnaghan equation. The theoretical structural visualization and charge distribution were plotted by the VESTA software (version 3.4.8) [23].

3. Results

Figure 2 shows the integrated XRD powder data taken at the maximum pressure of 241 GPa with pressure determined using the platinum EOS [12]. The difference curve shown below the powder pattern in Figure 2 resulted from a fit to the hexagonal structure to ReB_2 . The hexagonal phase of ReB_2 was found to be stable to the maximum pressure of 241 GPa. The measured lattice parameters at 241 GPa were $a = 2.586 \pm 0.004 \text{ \AA}$ and $c = 6.882 \pm 0.007 \text{ \AA}$. Platinum peaks in Figure 2 are labeled with asterisks (*) and indexed to a face-centered cubic lattice. The platinum lattice parameter at maximum pressure of 241 GPa was measured to be $a = 3.490 \pm 0.009 \text{ \AA}$.

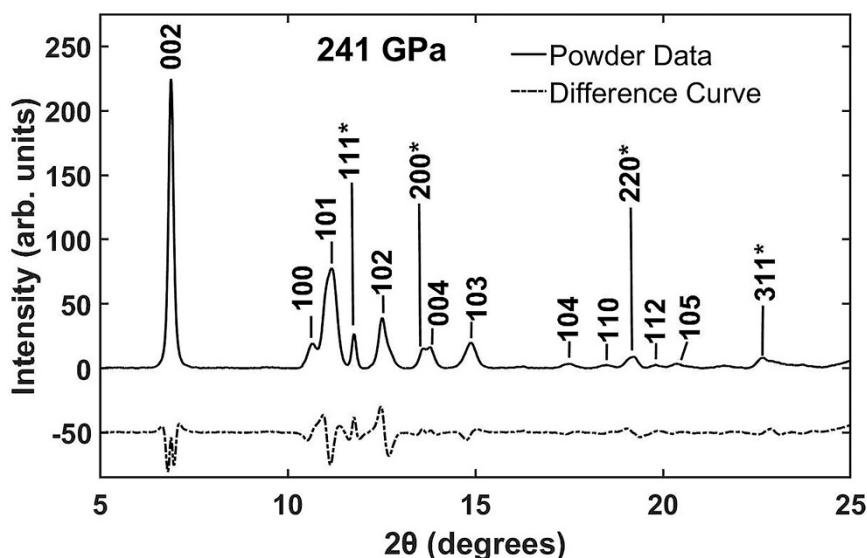


Figure 2. Powder diffraction of ReB_2 indexed to a hexagonal phase at a pressure of 241 GPa. Shown below the data curve is the difference curve as a result of Rietveld refinement. The platinum peaks (labeled with asterisk *) were indexed to a face-centered cubic phase and its measured volume was used in the calculation of pressure.

Figure 3a shows the volume compression for ReB_2 in two separate compression experiments with maximum pressures to 105 GPa in Experiment I (Expt. I) and 241 GPa in Experiment II (Expt. II). Figure 3b shows the volume compression for low-pressure data that exhibit uniaxial compression transitioning into non-hydrostatic compression at around 35 GPa. Both Expt. I and II showed transition zones from uniaxial compression to non-hydrostatic. For data points below the transition zone, the samples showed a fairly linear volumetric compression that is similarly seen in elastic samples before yielding to plastic deformation above the transition zone. It can be inferred from Figure 3 that the sample yielding at 30 GPa is a measure of the uniaxial compression strength, or the material's resistance to change before yielding. This is in agreement with the sample's average hardness, or its resistance to deformation being between 30 and 60 GPa [4–7]. The bulk modulus and its pressure derivative are taken from Equation (1) by fitting to the non-hydrostatic curve above 35 GPa, and they were determined to be $K_0 = 364$ GPa and $K_0' = 3.53$, respectively.

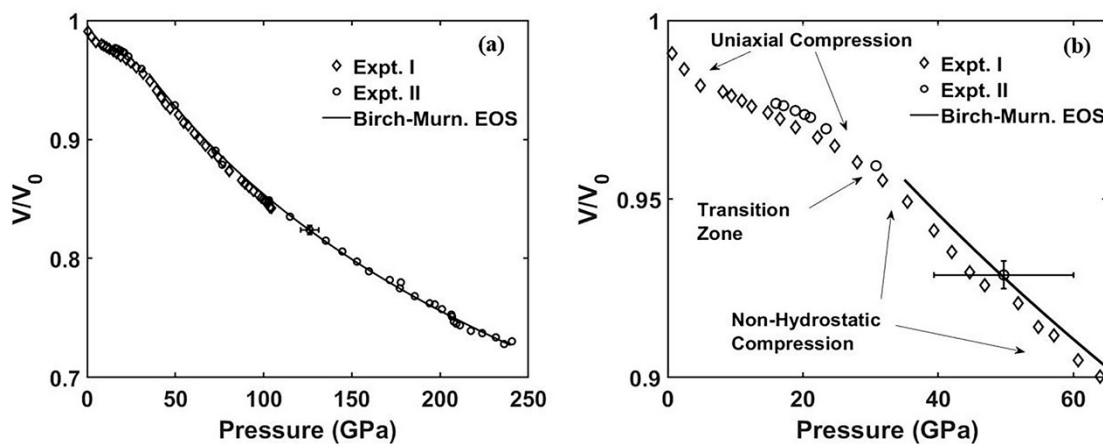


Figure 3. (a) Pressure-volume curve for Experiments I and II fitted with a 3rd order Birch–Murnaghan equation of state (EOS) above 35 GPa. (b) Pressure-volume curve for Experiments I and II for pressures below 65 GPa. Regions of uniaxial compression and non-hydrostatic compression are labeled along with the 3rd order Birch–Murnaghan equation of state (EOS) above 35 GPa.

The axial compression of the a and c lattice parameters for ReB_2 are shown in Figure 4, with the measured lattice parameters at 241 GPa being $a = 2.586 \pm 0.004 \text{ \AA}$ and $c = 6.882 \pm 0.007 \text{ \AA}$. For both experiments, the c -axis showed a strong incompressibility as $c/c_0 = 0.920 \pm 0.001$ at 241 GPa, not even 10% compression. In comparison, there was strong anisotropy between the a -axis and c -axis that persisted throughout the entirety of both experiments, and the anisotropy increased with pressure to maximum compression of $a/a_0 = 0.891 \pm 0.001$. The maximum volume compression at 241 GPa was measured to be $V/V_0 = 0.731 \pm 0.004$.

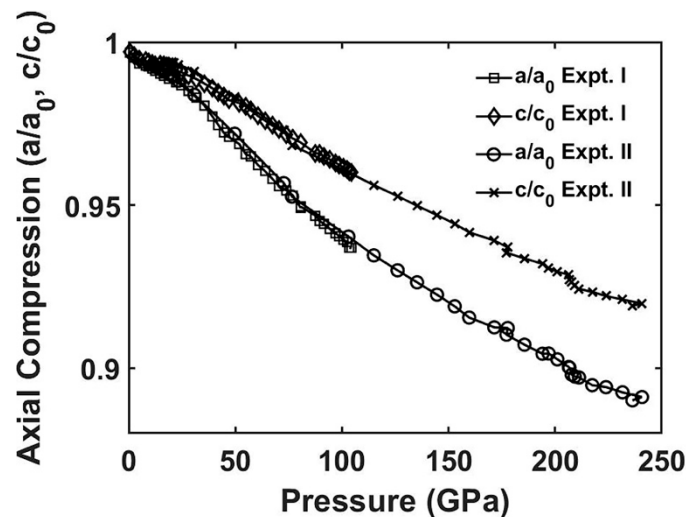


Figure 4. Axial compression of the a and c lattice parameters to 105 GPa for Experiment I and 241 GPa for Experiment II. The anisotropic compression is observed to the highest pressure of 241 GPa.

To simulate the high-pressure experiments, we performed structure relaxation DFT calculations with the GGA functional up to 250 GPa. The DFT-GGA axial and volume compressions simulated under hydrostatic pressure are shown in Figure 5a,b, respectively. The a/a_0 and c/c_0 curves with pressure are both concave up, suggesting that the upturn or concave down behavior observed experimentally at pressures between 5 and 35 GPa (Figure 3b) is related to a non-hydrostatic condition. Figure 5a also shows that the lattice parameter a is more compressible than c . In particular, the DFT-GGA value c/c_0 near 240 GPa is 0.919, which is in excellent agreement with the experiment. The DFT-GGA value a/a_0 near 240 GPa is 0.877, which underestimates the experimental value of 0.891. In addition to non-hydrostatic condition, the theory-experiment deviation at high pressure is most likely due to the employed GGA functional. In particular, compared with previous local density approximation (LDA) studies at 100 GPa [24], while in both LDA and GGA values $c/c_0 = 0.954$, the LDA ratio $a/a_0 = 0.932$ is larger than the GGA value of 0.928. Regardless of the functional being employed, it is clear that an anisotropic compression behavior persisted up to the maximum pressure under study: a/c began with 0.388 at ambient conditions and decreased monotonically to 0.370 (0.375) in theory (experiment) near 240 GPa.

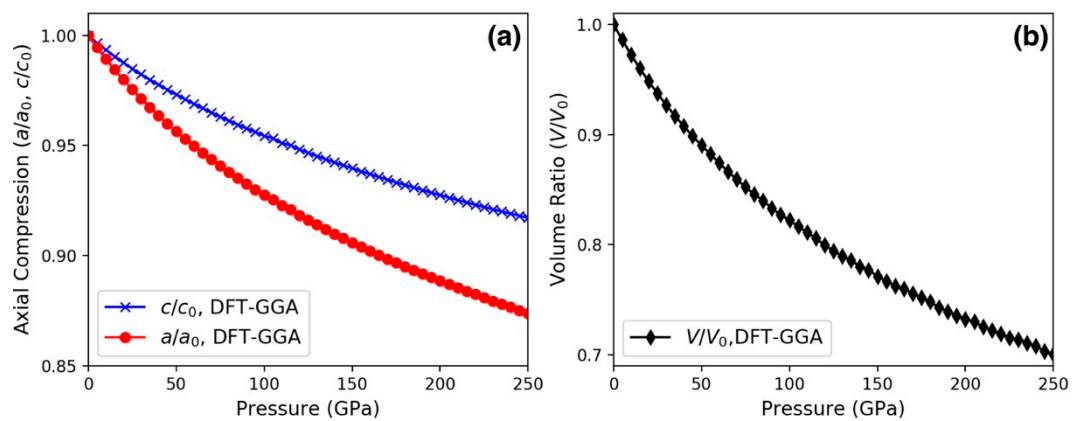


Figure 5. (a) Axial compression of the a and c lattice parameters computed by density functional theory (DFT) using the generalized gradient approximation (GGA) functional for ReB_2 under hydrostatic pressure up to 250 GPa. (b) Pressure-volume curve corresponding to (a).

4. Discussion

The addition of interstitial covalently bonded boron atoms to high-electron-density transition metals such as Re and Os has given a family of transition metal diborides with desirable mechanical properties. Re and Os , being one column away from each other on the periodic table, share similar properties, although Re has a slightly smaller electron density and Os has a higher hardness and incompressibility [25,26]. OsB_2 was shown to have a comparable bulk modulus (342–365 GPa) to ReB_2 , but ReB_2 is considered somewhat superior due to shorter metallic bonds [27,28]. There is also a noticeable difference between the brittleness and ductility of the two materials. Pugh [29] introduced the ratio between the shear modulus and the bulk modulus (G/K) to distinguish a material's ductile or brittle behavior. A low (high) G/K value is correlated with ductility (brittleness). Based on the elastic and plastic properties of pure polycrystalline simple metals, an empirical value of the brittle-to-ductile transition is 0.571. Figure 6a shows the bulk and shear moduli computed by DFT using the GGA functional. While both G and K are enhanced by pressure, the rate of increase for K is larger, indicating that the G/K decreases with pressure, as seen in Figure 6b. In particular, G/K changes from 0.762 at 0 GPa to 0.627 at 240 GPa. In comparison, the G/K value is substantially smaller in OsB_2 [30]. In our calculation, the G/K values for OsB_2 at 0 GPa and 240 GPa are respectively 0.528 and 0.478, both of which are below the critical brittle-to-ductile transition value 0.571, showing that OsB_2 is more ductile than ReB_2 . Another relevant quantity is the Poisson's ratio, which can be obtained by $(3K - 2G)/[2(3K + G)]$. Based on Frantsevich's rule [31], a material is brittle if its Poisson's ratio is less than $1/3$; otherwise, the material is ductile. Figure 6b also shows that the Poisson ratio for ReB_2 increases with pressure, indicating an enhanced ductility.

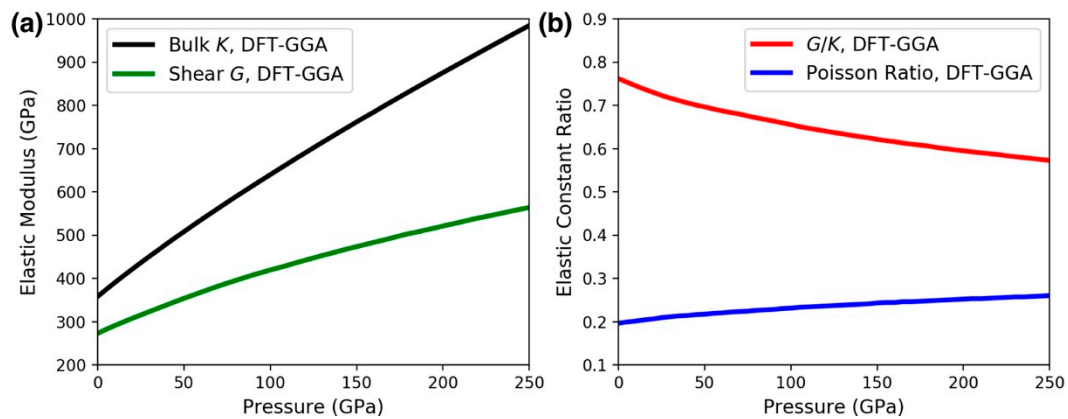


Figure 6. (a) Bulk (K) and shear (G) moduli for ReB_2 as a function of pressure. The elastic moduli were obtained using the elastic constants computed by density functional theory (DFT) with the generalized gradient approximation (GGA) functional and the Voigt–Reuss–Hill approximation. (b) The G/K ratio and the Poisson ratio = $(3K - 2G)/[2(3K + G)]$, showing that the material became more ductile with increasing pressure.

We next address the strong lattice anisotropy observed in ReB_2 . Interestingly, the hexagonal ReB_2 and orthorhombic OsB_2 both showed anisotropic behavior in lattice parameters, with the c -axis being the most incompressible [5,27]. The observed extreme anisotropy of ReB_2 shown in Figure 4 is likely attributed to the high electron density of Re and the high density of states (DOS) at the Fermi level (E_F) [4], which result in increased Coulomb repulsion with pressure. Figure 7a shows our computed DOS for ReB_2 at 0 GPa (top panel) and 240 GPa (bottom panel). The DOS plots indicate that at E_F (denoted by the vertical dashed red line), the spectra have a dominant contribution from the Re atom. At high pressure, the spectral contributions at E_F from Re and B atoms both increase, as seen in Figure 7b. The enhanced DOS also suggests an increased metallic bonding, or a reduced covalent bonding, which is consistent with the iso-surface charge density plots in Figure 8: at ambient conditions, ReB_2 possesses strong covalent bonds between B - B atoms. When external pressure increases, the hybridizations between Re - B and B - B atoms both increase, leading to an enhanced DOS at E_F and a reduced directional bonding. The increased Re - B bonding states near E_F also can lead to enhanced bulk and shear moduli at high pressure [32].

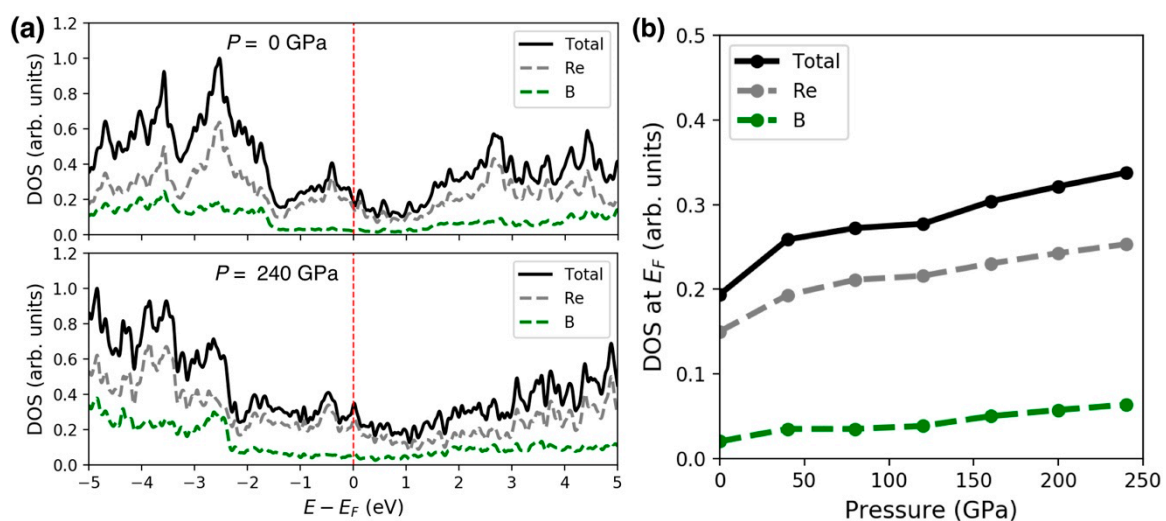


Figure 7. (a) ReB_2 density of states (DOS) plots at pressure $P = 0$ GPa (top) and 240 GPa (bottom), respectively. The Fermi level (E_F) is indicated by the vertical dashed red line. (b) DOS at E_F as a function of pressure.

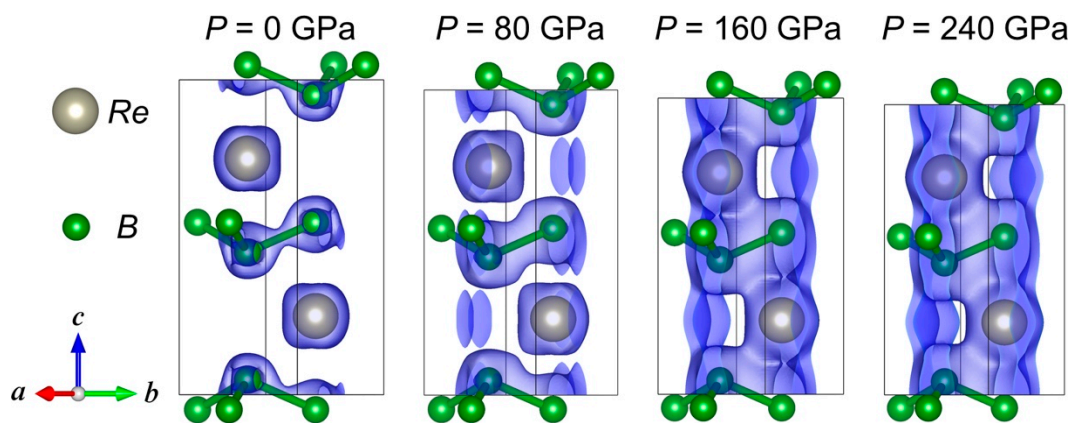


Figure 8. ReB_2 unit cells and iso-surfaces of charge density under external pressures up to 240 GPa. Iso-surface levels were set to be $0.1 a_0^{-3}$, with a_0 the Bohr radius. The calculations were based on the VASP software and its CHGCAR file, which contains the lattice vectors, atomic coordinates, the total charge density multiplied by the volume on the fine fast Fourier transform-grid, and the projector augmented wave one-center occupancies. The theoretical structural visualization and charge distribution were plotted by the VESTA software.

In the hexagonal phase of ReB_2 (with space group $P6_3/mmc$), the two Re atoms are located at Wyckoff positions $(1/3, 2/3, 1/4)$ and $(2/3, 1/3, 3/4)$, and the four B atoms are located at $(1/3, 2/3, \pm z)$ and $(2/3, 1/3, 1/2 \pm z)$, where z is 0.0476 (0.0452) for $P = 0$ (240) GPa. The Re and B atoms are aligned along the c -axis. Under compression, as seen in Figure 8, the electron density is centered along the Re - B bonds, which are parallel to the c -axis. The strong electron Coulomb repulsion between charge density distributed along the Re - B bond direction makes the material highly incompressible along the c -axis. A strong anisotropy between the crystal a and c lattice parameters also suggests that the highest hardness in ReB_2 single crystals is along the c -axis [5,33].

In addition to anisotropy in the lattice parameters, it is important to consider crystal elastic anisotropy, which is related to the occurrence of micro-cracks in materials [34,35]. Figure 9a shows the five independent elastic constants computed by DFT using the GGA functional for hexagonal ReB_2 as a function of pressure. It is seen that c_{11} and c_{33} are largely enhanced upon compression, compared to the other elastic constants. Also, c_{33} is larger than c_{11} , indicating that the c -axis is the least compressible. There are other ways to represent the level of elastic anisotropy of a material. In a hexagonal crystal, the following three parameters can be used [24,36]: $\Delta_p = c_{33}/c_{11}$, $\Delta_{s1} = (c_{11} + c_{33} - 2c_{13})/4c_{44}$, and $\Delta_{s2} = 2c_{44}/(c_{11} - c_{12})$. These three parameters would be equal to unity for isotropic compressibility. Figure 9b shows that the computed Δ_p , Δ_{s1} , and Δ_{s2} are all larger than 1 up to the maximum pressure under study. These results are consistent with previous lower-pressure theoretical studies [24,37], indicating a strong elastic anisotropy of ReB_2 , where its c -axis compressibility is smaller than that along the a -axis.

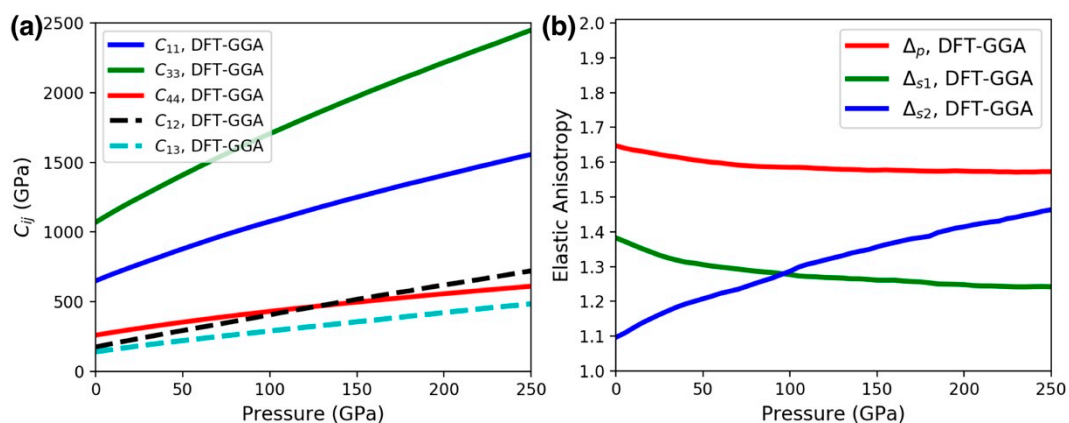


Figure 9. (a) The five independent elastic constants computed by density functional theory (DFT) with the generalized gradient approximation (GGA) functional for hexagonal ReB_2 as a function of pressure. (b) Parameters indicative of elastic anisotropy for a hexagonal crystal: $\Delta_p = c_{33}/c_{11}$, $\Delta_{s1} = (c_{11} + c_{33} - 2c_{13})/4c_{44}$, and $\Delta_{s2} = 2c_{44}/(c_{11} - c_{12})$. For isotropic compressibility, all parameters are equal to unity.

5. Conclusions

Ultrahigh non-hydrostatic compression studies were carried out on a superhard material ReB_2 for the first time to a pressure of 241 GPa. The equation of state determined from the non-hydrostatic pressure-volume curve above 35 GPa yielded a bulk modulus and pressure derivative of $K_0 = 364$ GPa and $K_0' = 3.53$, respectively. Substantial anisotropy of the lattice parameters was indicated to increase with pressure up to the maximum pressure, with $a/a_0 = 0.891$ and $c/c_0 = 0.919$ at 241 GPa, showing $\sim 3\%$ difference in axial compression. The results from density functional theory simulations for anisotropic compression, equation of state, and elastic constants were in good agreement with the experimental data. The superhard and ultra-incompressible features of ReB_2 render it a promising material for wide ranges of applications in extreme environments.

Author Contributions: K.C.B. and Y.K.V. conceived the project and performed high-pressure experiments. C.-M.L., W.-C.C., and C.-C.C. performed DFT calculations and contributed to theoretical analysis. Y.K.V. coordinated the development of the manuscript for publication. K.C.B., C.-C.C., and Y.K.V. prepared the original draft manuscript. All authors reviewed and edited the manuscript. All authors have read and agreed to the published version of the manuscript.

Funding: This research is funded by the U.S. National Science Foundation under Metals and Metallic Nanostructures program Grant No. DMR-1904164. Any opinions, findings, and conclusions or recommendations expressed in this material are those of the authors and do not necessarily reflect the views of the National Science Foundation.

Acknowledgments: Portions of this work were performed at HPCAT (Sector 16), Advanced Photon Source (APS), Argonne National Laboratory. HPCAT operations are supported by DOE-NNSA's Office of Experimental Sciences. The Advanced Photon Source is a U.S. Department of Energy (DOE) Office of Science User Facility operated for the DOE Office of Science by Argonne National Laboratory under Contract No. DE-AC02-06CH11357. The calculations were performed on the Frontera computing system at the Texas Advanced Computing Center. Frontera is made possible by National Science Foundation award OAC-1818253.

Conflicts of Interest: The authors declare no conflict of interest. The funders had no role in the design of the study; in the collection, analyses, or interpretation of data; in the writing of the manuscript, or in the decision to publish the results.

References

- Friedrich, A.; Winkler, B.; Juarez-Arellano, E.A.; Bayarjargal, L. Synthesis of Binary Transition Metal Nitrides, Carbides and Borides from the Elements in the Laser-Heated Diamond Anvil Cell and Their Structure-Property Relations. *Materials* **2011**, *4*, 1648–1692. [[CrossRef](#)] [[PubMed](#)]
- Gu, Q.; Krauss, G.; Steurer, W. Transition Metal Borides: Superhard versus Ultra-incompressible. *Adv. Mater.* **2008**, *20*, 3620–3626. [[CrossRef](#)]

3. Yeung, M.T.; Mohammadi, R.; Kaner, R.B. Ultraincompressible, Superhard Materials. *Annu. Rev. Mater. Res.* **2016**, *46*, 465. [[CrossRef](#)]
4. Zhou, W.; Wu, H.; Yildirim, T. Electronic, dynamical, and thermal properties of ultra-incompressible superhard rhenium diboride: A combined first-principles and neutron scattering study. *Phys. Rev. B* **2007**, *76*, 184113. [[CrossRef](#)]
5. Chung, H.-Y.; Weinberger, M.B.; Levine, J.B.; Cumberland, R.W.; Kavner, A.; Yang, J.-M.; Tolbert, S.H.; Kaner, R.B. Synthesis of Ultra-Incompressible Superhard Rhenium Diboride at Ambient Pressure. *Science* **2007**, *316*, 436–439. [[CrossRef](#)]
6. Chrzanowska, J.; Hoffman, J.; Denis, P.; Giżyński, M.; Moscicki, T. The effect of process parameters on rhenium diboride films deposited by PLD. *Surf. Coat. Technol.* **2015**, *277*, 15–22. [[CrossRef](#)]
7. Lazar, P.; Chen, X.-Q.; Podlucky, R. First-principles modeling of hardness in transition-metal diborides. *Phys. Rev. B* **2009**, *80*, 012103. [[CrossRef](#)]
8. Aleksandrov, I.V.; Goncharov, A.F.; Zisman, A.N.; Stishov, S.M. Diamond at high pressures: Raman scattering of light, equation of state, and highpressure scale. *Sov. Phys. JETP* **1987**, *66*, 384.
9. Kavner, A.; Armentrout, M.; Rainey, E.S.G.; Xie, M.; Weaver, B.E.; Tolbert, S.H.; Kaner, R.B. Thermoelastic properties of ReB₂ at high pressures and temperatures and comparison with Pt, Os, and Re. *J. Appl. Phys.* **2011**, *110*, 093518. [[CrossRef](#)]
10. Parka, C.; Popov, D.; Ikuta, D.; Lin, C.; Kenney-Benson, C.; Rod, E.; Bommannavar, A.; Shen, G. New developments in micro-X-ray diffraction and X-ray absorption spectroscopy for high-pressure research at 16-BM-D at the Advanced Photon Source. *Rev. Sci. Instrum.* **2015**, *86*, 072205. [[CrossRef](#)]
11. Toby, B.H.; Von Dreele, R.B. GSAS-II: The genesis of a modern open-source all purpose crystallography software package. *J. Appl. Crystallogr.* **2013**, *46*, 544–549. [[CrossRef](#)]
12. Yokoo, M.; Kawai, N.; Nakamura, K.G.; Kondo, K.-I.; Tange, Y.; Tsuchiya, T. Ultrahigh-pressure scales for gold and platinum at pressures up to 550 GPa. *Phys. Rev. B* **2009**, *80*, 104114. [[CrossRef](#)]
13. Hohenberg, P.; Kohn, W. Inhomogeneous Electron Gas. *Phys. Rev.* **1964**, *136*, B864. [[CrossRef](#)]
14. Born, M.; Oppenheimer, J.R. On the Quantum Theory of Molecules. *Ann. Phys.* **1927**, *389*, 457. [[CrossRef](#)]
15. Kohn, W.; Sham, L.J. Self-Consistent Equations Including Exchange and Correlation Effects. *Phys. Rev.* **1965**, *140*, A1133. [[CrossRef](#)]
16. Kresse, G.; Furthmüller, J. Efficiency of ab-initio total energy calculations for metals and semiconductors using a plane-wave basis set. *Comput. Mater. Sci.* **1996**, *6*, 15–50. [[CrossRef](#)]
17. Kresse, G.; Furthmüller, J. Efficient iterative schemes for ab initio total-energy calculations using a plane-wave basis set. *Phys. Rev. B* **1996**, *54*, 11169. [[CrossRef](#)]
18. Blöchl, P.E. Projector augmented-wave method. *Phys. Rev. B* **1994**, *50*, 17953–17979. [[CrossRef](#)]
19. Kresse, G.; Joubert, D. From ultrasoft pseudopotentials to the projector augmented-wave method. *Phys. Rev. B* **1999**, *59*, 1758. [[CrossRef](#)]
20. Perdew, J.P.; Burke, K.; Ernzerhof, M. Generalized Gradient Approximation Made Simple. *Phys. Rev. Lett.* **1996**, *77*, 3865. [[CrossRef](#)]
21. Monkhorst, H.J.; Pack, J.D. Special points for Brillouin-zone integrations. *Phys. Rev.* **1976**, *13*, 5188–5192. [[CrossRef](#)]
22. Hill, R. The elastic behavior of a crystalline aggregate. *Proc. Phys. Soc.* **1952**, *65*, 349. [[CrossRef](#)]
23. Momma, K.; Izumi, F. VESTA 3 for three-dimensional visualization of crystal, volumetric and morphology data. *J. Appl. Crystallogr.* **2011**, *44*, 1272–1276. [[CrossRef](#)]
24. Zhu, X.; Li, D.; Cheng, X. Elasticity properties of the low-compressible material ReB₂. *Solid State Commun.* **2008**, *147*, 301–304. [[CrossRef](#)]
25. Perreault, C.S.; Velisavljevic, N.; Vohra, Y.K. High-pressure structural parameters and equation of state of osmium to 207 GPa. *Cogent Phys.* **2017**, *4*, 1376899. [[CrossRef](#)]
26. Armentrout, M.M.; Kavner, A. Incompressibility of osmium metal at ultrahigh pressures and temperatures. *J. Appl. Phys.* **2010**, *107*, 093528. [[CrossRef](#)]
27. Cumberland, R.W.; Weinberger, M.B.; Gilman, J.J.; Clark, S.M.; Tolbert, S.H.; Kaner, R.B. Osmium Diboride, an Ultra-Incompressible Hard Material. *J. Am. Chem. Soc.* **2005**, *127*, 7264–7265. [[CrossRef](#)]
28. Hebbache, M.; Stuparević, L.; Živković, D. A new superhard material: Osmium diboride OsB₂. *Solid State Commun.* **2006**, *139*, 227–231. [[CrossRef](#)]
29. Pugh, S.F. Relation between the elastic moduli and the plastic properties of polycrystalline pure metals. *Philos. Mag.* **1954**, *45*, 823. [[CrossRef](#)]

30. Yang, J.-W.; Chen, X.-R.; Luo, F.; Ji, G.-F. First-principles calculations for elastic properties of OsB₂ under pressure. *Physica B* **2009**, *404*, 3608. [[CrossRef](#)]
31. Frantsevich, I.N. (Ed.) *Elastic Constants and Elastic Moduli of Metals and Insulators Handbook*; Naukova Dumka: Kiev, Ukraine, 1983.
32. Hao, X.; Wu, Z.; Xu, Y.; Zhou, D.; Liu, X.; Meng, J. Trends in elasticity and electronic structure of 5d transition metal diborides: First-principles calculations. *J. Phys. Condens. Matter* **2007**, *19*, 196212. [[CrossRef](#)]
33. Šimůnek, A. Anisotropy of hardness from first principles: The cases of ReB₂ and OsB₂. *Phys. Rev. B* **2009**, *80*, 060103. [[CrossRef](#)]
34. Ravindran, P.; Fast, L.; Korzhavyi, P.A.; Johansson, B.; Wills, J.; Eriksson, O. Density functional theory for calculation of elastic properties of orthorhombic crystals: Application to TiSi₂. *J. Appl. Phys.* **1998**, *84*, 4891. [[CrossRef](#)]
35. Hutchinson, J.W.; Tvergaard, V. Edge-Cracks in Single Crystals under Monotonic and Cyclic Loads. *Int. J. Fract.* **1999**, *99*, 81. [[CrossRef](#)]
36. Steinle-Neumann, G.; Stixrude, L.; Cohen, R.E. First-principles elastic constants for the hcp transition metals Fe, Co, and Re at high pressure. *Phys. Rev. B* **1999**, *60*, 791. [[CrossRef](#)]
37. Hao, X.; Xu, Y.; Wu, Z.; Zhou, D.; Liu, X.; Cao, X.; Meng, J. Low-compressibility and hard materials ReB₂ and WB₂: Prediction from first-principles study. *Phys. Rev. B* **2006**, *74*, 224112. [[CrossRef](#)]



© 2020 by the authors. Licensee MDPI, Basel, Switzerland. This article is an open access article distributed under the terms and conditions of the Creative Commons Attribution (CC BY) license (<http://creativecommons.org/licenses/by/4.0/>).